ACCSCIENCE PUBLISHING

Journal of Seismic Exploration

ARTICLE

Rayleigh-wave dispersion-curve inversion using the bounty hunter optimizer

Zhiying Liao, Miaojun Sun*, Jian Xu, and Ping Xu

Zhejiang Huadong Geotechnical Investigation & Design Institute Co. Ltd., Powerchina Huadong Engineering Co., Ltd., Hangzhou, Zhejiang, China

Abstract

Rayleigh-wave dispersion inversion estimates near-surface shear-wave velocity and layer thickness, but its nonlinear, multimodal, and non-unique nature can hinder global optimization and repeatability. This study applies the bounty hunter optimizer (BHO) to fundamental-mode and joint multimode inversion. BHO combines oversampling and *K*-means initialization, cooperative group search, dynamic task allocation, Explorpolis filtering, and quantum probability rotation selection. Performance is evaluated using two benchmark functions, three synthetic layered models, prescribed 10% uniform-random perturbations, comparisons with other optimizers, and field data from Wyoming, United States. BHO yielded the lowest objective-function values in the benchmark and Model A comparisons, and recovered the principal velocity features of the synthetic models. Across noise-free and perturbed tests, median models preserved these features, although empirical parameter ranges broadened for more complex models. Incorporating correctly identified higher modes reduced the errors of most synthetic-model parameters. For the field data, the mean multimode model from 20 independent runs agreed well with the borehole velocity profile between 0 and 13 m depth, and median parameter estimates were close to the means. BHO achieved greater accuracy and repeatability at a higher computational cost under the tested settings. An overparameterized test further illustrates the distinction between dispersion fit and model recovery. These results support BHO as a global optimizer for the one-dimensional isotropic layered models examined here, without establishing uniqueness or performance under realistic field-data uncertainty.

Keywords: Rayleigh wave; Dispersion-curve inversion; Bounty hunter optimizer; Shear-wave velocity; Multimode dispersion; Global optimization

***Corresponding author:**
Miaojun Sun
(sun_mj2@163.com)

Citation: Liao Z, Sun M, Xu J, Xu P. Rayleigh-wave dispersion-curve inversion using the bounty hunter optimizer. *J Seismic Explor.* doi: 10.36922/JSE026350168

Received: August 30, 2026

Revised: October 10, 2026

Accepted: October 16, 2026

Published online: November 19, 2026

Copyright: © 2026 Author(s). This is an Open-Access article distributed under the terms of the Creative Commons Attribution License, permitting distribution, and reproduction in any medium, provided the original work is properly cited.

Publisher's Note: AccScience Publishing remains neutral with regard to jurisdictional claims in published maps and institutional affiliations.

1. Introduction

Rayleigh waves are elastic surface waves generated by coupled P- and shear-vertical-wave motion near a free surface. Their energy is concentrated near the ground surface and propagates along it. Rayleigh first derived their propagation characteristics in 1885, establishing the theoretical basis for elastic surface-wave analysis.[1] In a horizontally layered elastic medium, Rayleigh-wave velocity depends on both frequency and the elastic properties of the medium and is therefore dispersive. Classical transfer-matrix methods, represented by the Thomson–Haskell formulation, and subsequent global-

matrix approaches established the basis for modeling elastic-wave propagation in layered media.[2-4] In the present study, Rayleigh-wave dispersion is calculated using the generalized reflection/transmission coefficient method developed by Chen.[5] This method computes normal-mode phase velocities and eigenfunctions for a multilayered isotropic half-space while excluding exponentially growing terms, thereby improving numerical stability at high frequencies. More general formulations, such as the six-dimensional Cauchy formalism, can describe wave dispersion in multilayered media with arbitrary elastic anisotropy.[6] The present study focuses on evaluating the bounty hunter optimizer (BHO) under a one-dimensional isotropic parameterization and does not address highly layered anisotropic models. Because different frequencies sample different depths and material volumes, measured dispersion curves constrain the subsurface shear-wave velocity structure; shear-wave velocity and layer thickness are the dominant parameters in most near-surface inversions.[7-10] Active-source multichannel analysis of surface waves is non-invasive, efficient, and can resolve shallow structure; consequently, it has been used for engineering-site characterization, seismic-site-response assessment, pavement and infrastructure evaluation, and detection of shallow anomalies.[11-13] Reliable conversion of surface-wave observations into subsurface structure depends critically on the accuracy and stability of the dispersion inversion. Robust estimation of the shear-wave velocity profile and layer parameters is therefore essential to realizing the full interpretive value of surface-wave surveys.[13,14]

Surface-wave dispersion analysis generally comprises seismic acquisition, dispersion-image construction and picking, model parameterization, and inversion. The central task is to identify, within a prescribed parameter space, a velocity model whose calculated dispersion response best matches the observations.[13-16] The mapping between model parameters and Rayleigh-wave dispersion is highly nonlinear and commonly exhibits parameter coupling, multiple extrema, and non-uniqueness. Limited low-frequency information, trade-offs between shallow and deep parameters, and observational noise further increase sensitivity to the starting model, parameter bounds, and objective function.[17,18] Local approaches, including linearized iteration, damped least squares, and Occam-type inversion, are computationally efficient but normally require a suitable initial model and gradient information. They may converge to a local solution when velocity reversals or complex layering are present.[19,20] To reduce dependence on the initial model, neighborhood algorithms, simulated annealing, genetic algorithms, particle swarm optimization, and other global or population-based methods have been applied to dispersion inversion.[21-27] Such methods improve exploration of the model space, but complex, non-convex objective functions can still create an unfavorable exploration-exploitation balance, high computational cost, or poor run-to-run stability. Improving search efficiency, convergence, and reliability therefore remains an important objective in surface-wave inversion.

To address these limitations, this study applies the BHO, a metaheuristic introduced by Yu *et al.*[28] in 2026, to Rayleigh-wave dispersion-curve inversion. BHO uses a decentralized population structure and adaptive exploration–exploitation mechanisms intended to reduce premature convergence in multimodal search spaces. Its numerical behavior is first examined using two penalized benchmark functions. Inversion performance is then evaluated with three representative layered-earth models under noise-free and noisy conditions. BHO is compared with the whale optimization algorithm (WOA), particle swarm optimization (PSO), and artificial protozoa optimizer (APO), after which it is applied to field surface-wave data from Wyoming, United States. The synthetic and field examples are used to assess convergence, recovery accuracy, repeatability, robustness to random perturbations, and the value of higher-mode constraints.

2. Methodology

2.1. Bounty hunter optimizer: Principles and search strategy

The BHO was proposed by Yu *et al.*[28] as a metaheuristic inspired by the pursuit process of a bounty-hunter organization: intelligence gathering, task deployment, cooperative division of labor, and target capture. Unlike methods driven by population means, BHO uses decentralized position updates based on local differences and random perturbations. This design is intended to reduce center bias and population collapse. The four computational stages are summarized below.

2.1.1. Intelligence gathering

Before the search begins, BHO constructs a broad set of candidate clues. Instead of generating only N random individuals, it first samples a dimensionless candidate set of size 10 N uniformly from the unit hypercube $[0, 1]^D$. These normalized candidates correspond to physical model parameters through the component-wise transformation (**Equation 1**):

$$X = L + (U - L) \odot z \tag{1}$$

where X is a D-component candidate vector in physical parameter space, z is its dimensionless normalized vector,

N is the population size, D is the model-space dimension, L and U are the component-wise lower and upper parameter-bound vectors, respectively, and $\odot$ denotes element-wise multiplication.

2.1.2. Task deployment

After the candidate clues have been generated, BHO applies K-means clustering to the dimensionless candidate matrix in $[0, 1]^D$. Squared Euclidean distance is used as the clustering metric. The N resulting centroids are then mapped component-wise to the physical parameter space and used as the initial hunter population. Because clustering is completed before this mapping, layer thickness and shear-wave velocity have the same numerical range during initial representative selection, and neither parameter type is weighted according to its physical unit or numerical magnitude. Following the original BHO procedure, a separate K-means step subsequently assigns the initialized hunters to N_{group} pursuit groups. This second step assigns group membership and does not generate or reposition the initial candidates (**Equation 2**):

$$X_0 = \text{K-means}\left(X, N\right), \quad X_0 = \left[X_0^{\,1}, X_0^{\,2}, X_0^{\,3}, ..., X_0^{\,N}\right]^T \tag{2}$$

where X_0 is the initial hunter population, $X_0^{\,i}$ is the initial position of hunter i, K-means$(\cdot)$ is the K-means operation, and N_{group} is the number of pursuit groups. Intelligence gathering and task deployment together form the decentralized initialization stage of BHO: several dispersed groups search concurrently instead of evolving around a single mean location.

2.1.3. Cooperative division of labor

During groupwise tracking, hunters are dynamically assigned based on their within-group rank. Better-ranked hunters conduct a thorough search guided by the global best, group best, and personal historical best positions. Lower-ranked hunters perform a rough search: a reference hunter is selected randomly from the same group, movement is directed toward or away from that reference according to their relative quality, and a random perturbation expands the search region. Local exploitation and broader exploration are therefore retained within the same iteration. The thorough- and rough-search updates are (**Equations 3–6**):

$$s_i^k = 1\left\{R_{h,i}^{\;\;k} \le r_h^k\right\} \tag{3}$$

$$\begin{aligned} X_{i,j}^{k,\text{test}} &= X_{i,j}^k + m_i^k \times \\ &(c_{1,i}^k \times \text{rand} \times \left(X_{\text{best},j}^k - X_{i,j}^k\right) \\ &+ c_{2,i}^k \times \text{rand} \times \left(X_{\text{best},j}^{k,g} - X_{i,j}^k\right) \\ &+ c_{3,i}^k \times \text{rand} \times \left(X_{i,j}^{\text{best}} - X_{i,j}^k\right)) \end{aligned} \tag{4}$$

$$X_{i,j}^{k,\text{rough}} = X_{i,j}^k \pm \text{rand} \times \left(X_{r,j}^{k,g} - X_{i,j}^k\right) \tag{5}$$

$$X_{i,j}^{k,\text{test}} = X_{i,j}^{k,\text{rough}} \pm m_i^k \times \text{rand} \times X_{i,j}^{k,\text{rough}} \tag{6}$$

where s_i^k is the search mode of hunter i at iteration k, $R_{h,i}^{\;\;k}$ is its within-group rank, and $r_h^{\,k}$ is the switching threshold. A thorough search is used when $s_i^k = 1$; otherwise, a rough search is performed. $X_{i,j}^{\;\;k}$, $X_{i,j}^{k,\text{test}}$, and $X_{i,j}^{k,\text{rough}}$ denote the current, trial, and intermediate rough-search positions, respectively; m_i^k is the movement factor; $X_{\text{best},j}^{\;\;k}$, $X_{\text{best},j}^{k,g}$, and $X_{i,j}^{\text{best}}$ are the jth components of the global, group, and personal historical best positions; $X_{r,j}^{k,g}$ is a randomly selected reference in the best group; $c_{1,i}^{\;\;k}$, $c_{2,i}^{\;\;k}$, and $c_{3,i}^{\;\;k}$ are adaptive weights; and rand is a uniform random number in [0, 1].

After cooperative searching, BHO filters old and new clues using the Explorpolis rule proposed by Yu *et al.*[28] in the original BHO framework. This is its second core mechanism. A trial solution that does not immediately improve fitness may still be retained if the elite set contains no individual that is both better in objective value and closer in normalized distance. Spatially complementary candidates can thus survive, reducing premature concentration in a single region. The Explorpolis criterion is shown in **Equations 7** and **8**:

$$TD_i^k = \frac{\sqrt{\sum_{j=1}^{D}\left(\dfrac{X_{\text{new},j}^{k+1} - X_{i,j}^k}{U_j - L_j}\right)^2}}{D} \tag{7}$$

$$\text{TD}\left(X_{\text{test}}, S\right) = \min_{X_i \in S}\left\|\frac{X_{\text{test}} - X_{\text{old}}}{U - L}\right\|_2 \tag{8}$$

where $\text{TD}_i^{\,k}$ is the normalized distance between individual i and an elite solution, $X_{\text{new},j}^{\;\;k+1}$ is the jth component of an updated elite solution, S is the elite set, and X_{test} is a trial solution.

2.1.4. Target capture

As high-quality clues accumulate, BHO narrows the search and concentrates resources in promising regions. A hunter that repeatedly remains near the bottom of its group is classified as inefficient and reassigned to a group with greater cumulative contribution. Reassignment is implemented by quantum probability rotation selection (QPRS), the third core mechanism. QPRS represents group-selection states as continuous probability amplitudes and smoothly adjusts selection pressure through a quantum rotation gate, reducing scale sensitivity and variance compared with conventional roulette-wheel selection. The reassignment and probability updates are shown in **Equations 9–11**:

$$X_{i,j}^{k,\text{test}} = X_{i,j}^{k} + m_i^k \times (c_{1,i}^k \times \text{rand} \times \left(X_{\text{best},j}^k - X_{i,j}^k\right) + c_{2,i}^k \times \text{rand} \times \left(X_{\text{best},j}^{k,g'} - X_{i,j}^k\right) + c_{3,i}^k \times \text{rand} \times \left(X_{\text{better},j}^{\text{best},g'} - X_{i,j}^k\right)) \quad (9)$$

$$\alpha_1^2 + \beta_1^2 = 1 \quad (10)$$

$$\begin{bmatrix} \alpha_1' \\ \beta_1' \end{bmatrix} = \begin{bmatrix} \cos(\theta) & -\sin(\theta) \\ \sin(\theta) & \cos(\theta) \end{bmatrix} \begin{bmatrix} \alpha_1 \\ \beta_1 \end{bmatrix} \quad (11)$$

where $X_{\text{best},j}^{k,g'}$ is the jth component of the best position in the newly assigned group; $X_{\text{better},j}^{\text{best},g'}$ is the historical best component of a superior member of that group; α_1 and β_1 are probability amplitudes for selecting the best group; α_1' and β_1' are the updated amplitudes; and θ is the quantum rotation angle. Reassignment and progressive step-size contraction allow BHO to surround and refine promising regions. Figure 1 illustrates the search and individual-update mechanisms.[28]

2.2. Benchmark-function tests

The BHO was compared with APO,[29] WOA,[30] PSO, northern goshawk optimization,[31] Fourier transform optimization,[32] and artificial rabbits optimization.[33] The F_{12} and F_{13} high-dimensional nonlinear penalized functions were selected. Both contain periodic sine terms, coupling between adjacent variables, and boundary penalties, creating many local minima. F_{12} imposes a fourth-order penalty when $|x_i| > 10$ and has the global minimizer $x^* = (-1,\ldots,-1)$, whereas F_{13} has a narrower unpenalized interval, imposes a fourth-order penalty when $|x_i| > 5$, and has $x^* = (1,\ldots,1)$. Both theoretical optima are zero. For a consistent comparison, every algorithm used a population of 50 and 1,000 iterations; Table 1 statistics were calculated from 10 independent runs. The benchmark functions are (**Equations 12–15**):

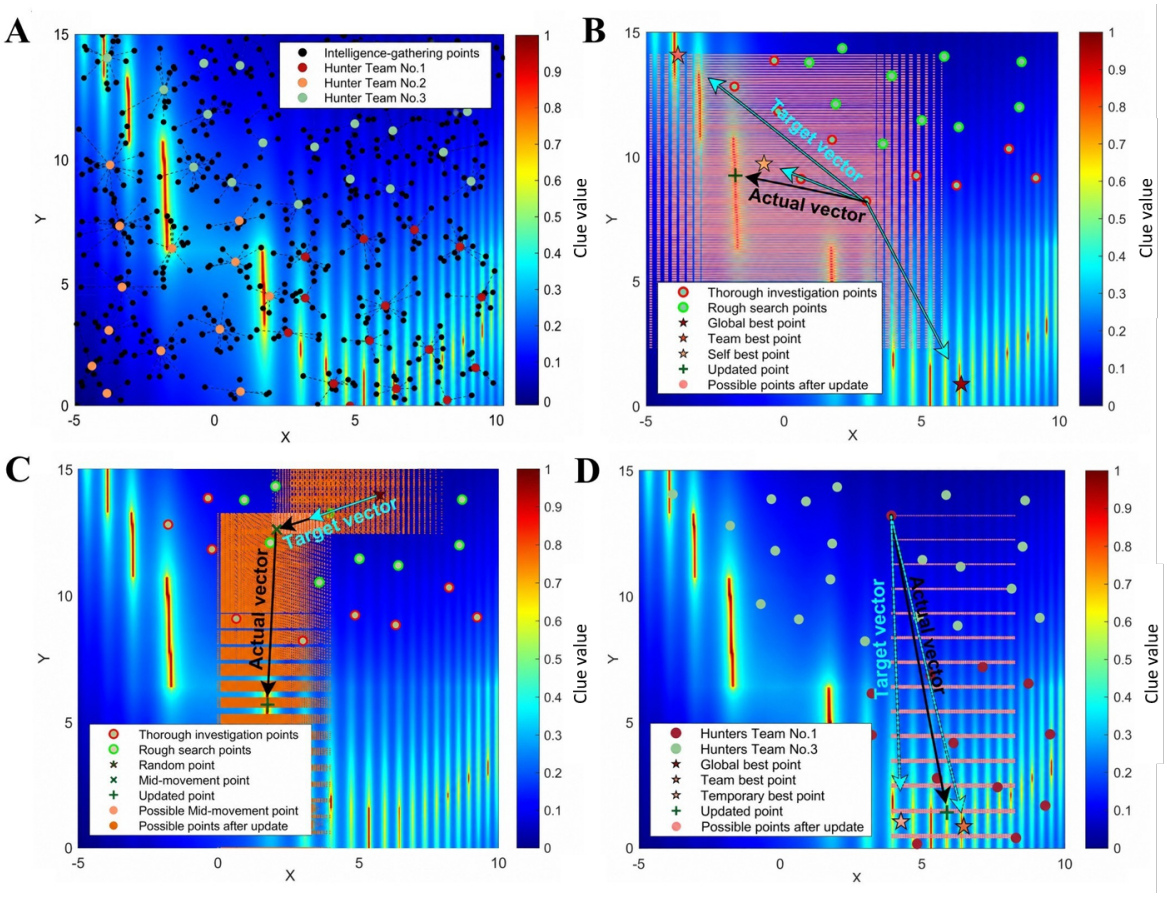

Figure 1. Bounty hunter optimizer (BHO) search and individual-update mechanisms. (A) Initialization and task deployment. (B) Thorough search. (C) Rough search. (D) Hunter reassignment.

$$F_{12}(x)=\frac{\pi}{n}[10\sin^2(\pi y_1)+\sum_{i=1}^{n-1}(y_i-1)^2 \left[1+10\sin^2(\pi y_{i+1})\right]+(y_n-1)^2] +\sum_{i=1}^{n}u(x_i,10,100,4) \tag{12}$$

$$F_{13}(x)=0.1[\sin^2(3\pi x_1)+\sum_{i=1}^{n-1}(x_i-1)^2 \left[1+\sin^2(3\pi x_{i+1})\right]+(x_n-1)^2 \left[1+\sin^2(2\pi x_n)\right]] +\sum_{i=1}^{n}u(x_i,5,100,4) \tag{13}$$

$$u(x_i,a,k,m)=\begin{cases}k(x_i-a)^m, & x_i>a\\ 0, & -a\le x_i\le a\\ k(-x_i-a)^m, & x_i<-a\end{cases} \tag{14}$$

$$y_i=1+\frac{1}{4}(x_i+1) \tag{15}$$

As shown in Figure 2 and Table 1, the BHO convergence curves for both functions decrease continuously and reach the lowest final objective values. For F_{12}, the best value, mean, and standard deviation are 1.01×10^{-23}, 3.63×10^{-15}, and 1.09×10^{-14}, respectively. For F_{13}, the corresponding values are 1.14×10^{-23}, 1.26×10^{-13}, and 2.05×10^{-13}. BHO therefore outperforms the other algorithms for these tests. Its mean error is approximately two orders of magnitude smaller than the second-best Fourier transform optimization result, indicating high numerical accuracy and good repeatability on the two penalized functions.

2.3. Inversion parameters and objective functions

In this study, forward dispersion curves for all synthetic models were calculated using the generalized reflection/transmission coefficient method developed by Chen.[5] For each frequency, this method solves the normal-mode eigenvalue problem in a horizontally layered, isotropic elastic half-space to obtain the modal phase velocities. The method combines layerwise reflection and transmission coefficients and excludes exponentially growing terms, improving numerical stability at high frequencies. Accordingly, the present implementation assumes isotropic layers described by density, P-wave velocity, S-wave velocity, and thickness.

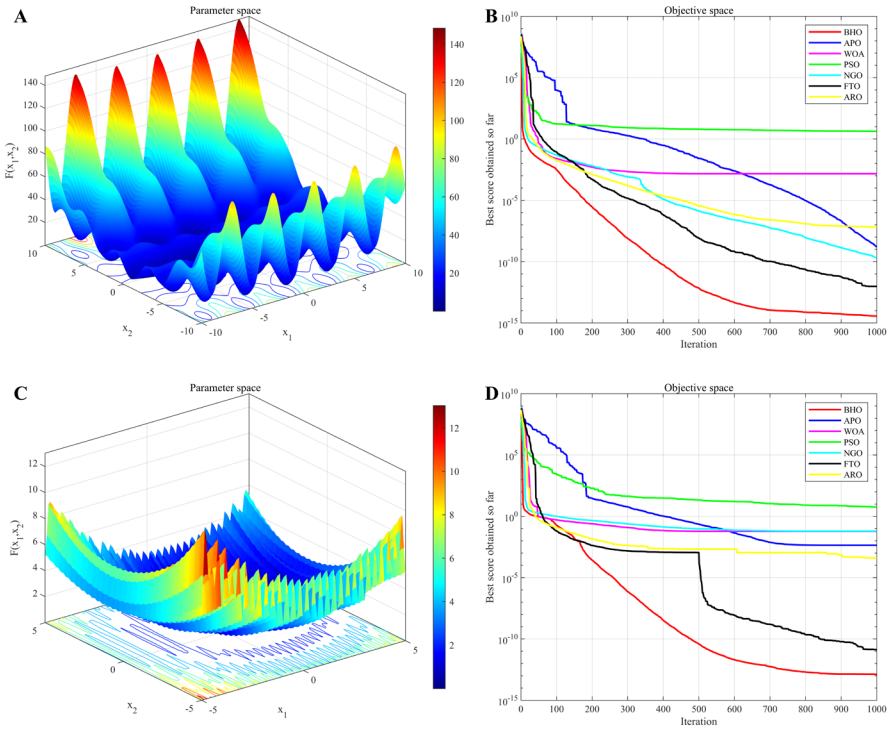

Figure 2. Benchmark functions and convergence histories. (A, C) F_{12} and F_{13} response surfaces. (B, D) Convergence curves of the tested algorithms. Abbreviations: APO: Artificial protozoa optimizer; ARO: Artificial rabbits optimization; BHO: Bounty hunter optimizer; FTO: Fourier transform optimization; NGO: Northern goshawk optimization; PSO: Particle swarm optimization; WOA: Whale optimization algorithm.

Table 1. Numerical results for the benchmark functions

Function	Statistic	BHO	APO	WOA	PSO	NGO	FTO	ARO
	Best	1.01E−23	1.69E−10	2.27E−04	1.79E+0	3.73E−11	3.72E−13	1.98E−08
F_{12}	Mean	3.63E−15	1.60E−09	1.50E−03	4.27E+0	2.07E−10	9.49E−13	6.80E−08
	Standard	1.09E−14	1.26E−09	3.44E−3	1.96E+0	2.02E−10	3.38E−13	3.52E−08
	Best	1.14E−23	1.17E−08	7.63E−03	2.56E+0	5.22E−08	6.58E−12	1.03E−07
F_{13}	Mean	1.26E−13	4.39E−03	6.00E−02	5.77E+0	6.16E−02	1.33E−11	3.81E−04
	Standard	2.05E−13	5.67E−03	4.08E−02	5.47E+0	6.82E−02	5.46E−12	1.20E−03

Abbreviations: APO: Artificial protozoa optimizer; ARO: Artificial rabbits optimization; BHO: Bounty hunter optimizer; FTO: Fourier transform optimization; NGO: Northern goshawk optimization; PSO: Particle swarm optimization; WOA: Whale optimization algorithm.

Fundamental-mode dispersion is commonly used because it is energetic, readily identified, and comparatively easy to pick. Higher modes, however, can improve resolution and reduce non-uniqueness when they are identified reliably. This study therefore considers both fundamental-mode and multimode inversion. For the layered models examined here, shear-wave velocity (V_S) and layer thickness (H) are treated as unknowns. The treatment of the other elastic parameters differs between the synthetic and field-data inversions. For the synthetic inversions, P-wave velocity (V_P) and density are fixed at their prescribed values, whereas Poisson's ratio is a derived quantity that varies with the candidate V_S. For the field-data inversions, Poisson's ratio (ν) and density are fixed, and V_P is recalculated for each candidate model according to **Equation 16**:

$$V_P = V_S\sqrt{\frac{2(1-\nu)}{1-2\nu}} \tag{16}$$

For the baseline synthetic inversions in Sections 3.1–3.4, the parameter bounds were set to ±50% of the true values. The distinct search bounds used for the overparameterized test are specified in Section 3.5. BHO uses a population of 30 and a maximum of 200 iterations. Each example was inverted 20 times, and repeated-run variability is reported alongside the representative results. Section 3.5 identifies the representative model as the one with the lowest final dispersion misfit because the parameter-mean model does not provide a comparably close fit in that test. The best-fitting solution was defined as the run with the lowest final objective-function value. The ensemble of recovered parameters was summarized using the component-wise median and empirical 5th–95th percentile ranges. The mean responses and models were retained in the figures only as visual summaries of the repeated inversions. The percentile ranges characterize stochastic run-to-run variability conditional on the fixed data, parameterization, search bounds, and objective function. They should not be interpreted as Bayesian credible intervals or posterior distributions.

For fundamental-mode inversion, the root-mean-square difference between the calculated and reference phase velocities was minimized (**Equation 17**):

$$P_0(m) = \sqrt{\frac{1}{N_0}\sum_{i\in\Omega_0}(v_{i,0}^{\text{inv}} - v_{i,0}^{\text{true}})^2} \tag{17}$$

where m is the model-parameter vector; $P_0(m)$ is the fundamental-mode objective; $v_{i,0}^{\text{inv}}$ and $v_{i,0}^{\text{true}}$ are the calculated and reference fundamental-mode phase velocities at frequency index i; Ω_0 is the set of valid fundamental-mode frequencies; and $N_0 = |\Omega_0|$ is the number of valid data points.

For joint inversion of the fundamental and higher modes, all valid phase-velocity observations were included in a single objective function (**Equation 18**):

$$P_{\text{multi}}(m) = \sqrt{\frac{\sum_{j=0}^{p}\sum_{i\in\Omega_j}(v_{i,j}^{\text{inv}} - v_{i,j}^{\text{true}})^2}{\sum_{j=0}^{p}N_j}} \tag{18}$$

where $P_{\text{multi}}(m)$ is the multimode objective; j is the mode index, with $j = 0$ for the fundamental mode and $j = 1,2,\ldots, p$ for higher modes; p is the highest mode included; $v_{i,j}^{\text{inv}}$ and $v_{i,j}^{\text{true}}$ are the calculated and reference phase velocities for mode j at frequency index i; Ω_j is the set of valid frequencies for mode j; N_j is the corresponding number of valid observations; and the denominator is the total number of observations across all included modes. No additional frequency- or mode-dependent weights were applied. Consequently, each valid mode-frequency observation

contributes equally to the squared-error sum, whereas the aggregate contribution of mode j is proportional to N_j. Only observations in Ω_j were included in the objective function, and missing or invalid observations did not contribute.

3. Synthetic model results

Three four-layer, horizontally stratified models were constructed to test BHO under different near-surface velocity structures (Table 2). Each model contains three finite layers over a half-space, with a total thickness of 12 m. Model A has monotonically increasing V_S, P-wave velocity, and density and was used to assess baseline accuracy. Model B contains a low-velocity layer: V_S decreases from 330 m/s in layer 2 to 220 m/s in layer 3. Model C contains a high-velocity layer: V_S increases to 440 m/s in layer 2, then decreases to 280 m/s in layer 3. These models tested the recovery of velocity reversals, local high-velocity layers, and strong interfaces. Dispersion curves were sampled from 1 to 100 Hz at 3 Hz intervals, giving 34 frequency points.

3.1. Noise-free synthetic inversions

Noise-free data from Models A–C were inverted first. Twenty independent runs were used to assess search stability and repeatability. Figure 3A, 3C, and 3E shows dispersion fits for Models A, B, and C. Cyan curves represent the calculated responses from the 20 runs, blue circles show the reference dispersion, and the red dashed curve is the mean response. Figure 3B, 3D, and 3F shows the corresponding V_S models. Light-blue shading denotes the search bounds, cyan lines denote individual inversions, the blue line with circles is the true model, and the red dashed line with triangles is the mean model. Table 3 reports the true values, best-fitting estimates, component-wise medians, and empirical 5th–95th percentile ranges of the recovered parameters. The best-fitting solution was defined as the run with the lowest final objective-function value.

The BHO fits the noise-free dispersion data closely for all three models (Figure 3). The 20 calculated dispersion curves formed compact ensembles and nearly coincided with the reference responses, indicating stable repeated searches. The best-fitting solutions for Models A, B, and C were obtained in runs 11, 12, and 17, with final objective-function values of 2.50×10^{-3}, 8.14×10^{-3}, and 3.57×10^{-3}, respectively. For Model A, both the best-fitting and median estimates were nearly identical to the true H and V_S values. For Model B, the median estimates of V_{S2} and V_{S3} were 330.551 and 221.422 m/s, respectively, preserving the low-velocity layer in the third layer. For Model C, the corresponding median estimates were 438.092 and 278.683 m/s, successfully recovering the high-velocity second layer and the subsequent velocity decrease.

The empirical parameter distributions broaden progressively from Model A to Models B and C, particularly

Table 2. Model parameters and inversion bounds for Models A–C

Model	Layer	Model parameters				Search bounds	
		V_S (m/s)	V_P (m/s)	ρ (g/cm^3)	H (m)	V_S (m/s)	H (m)
A	1	180	400	1.72	3	90–270	1.5–4.5
	2	260	570	1.84	4	130–390	2–6
	3	380	800	1.98	5	190–570	2.5–7.5
	4	560	1180	2.16	∞	280–840	∞
B	1	200	440	1.76	3	100–300	1.5–4.5
	2	330	730	1.98	5	165–495	2.5–7.5
	3	220	500	1.84	4	110–340	2–6
	4	560	1200	2.18	∞	280–840	∞
C	1	180	400	1.70	3	90–270	1.5–4.5
	2	440	930	2.08	4	220–660	2–6
	3	280	610	1.88	5	140–460	2.5–7.5
	4	600	1280	2.22	∞	300–900	∞

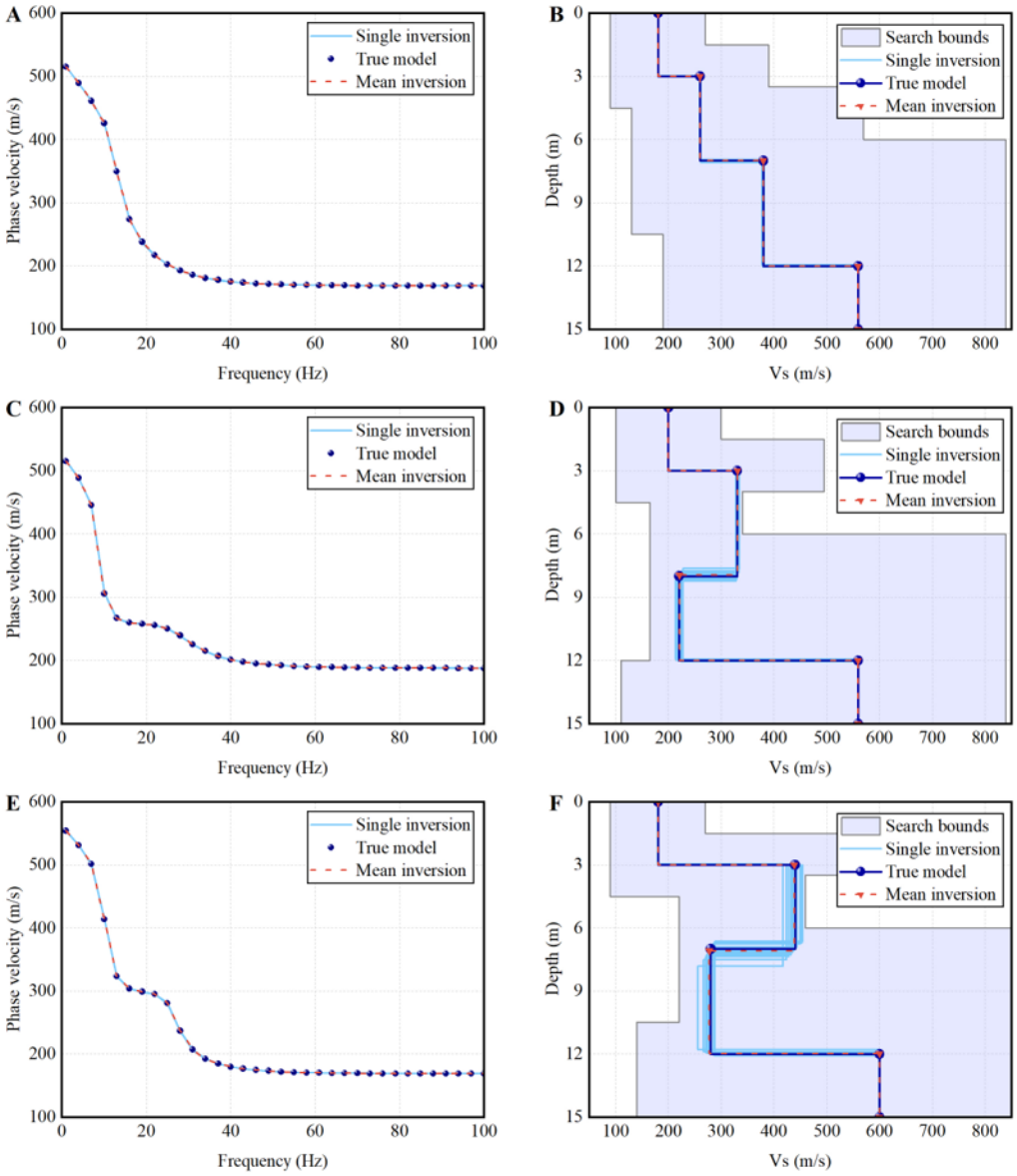

Figure 3. Noise-free inversion results for Models A–C. (A, C, E) Dispersion curves. (B, D, F) Shear-wave velocity profiles.

for intermediate-layer velocities and thicknesses (Table 3). Nevertheless, the true parameter values remained within the empirical 5th–95th percentile ranges for all three models, and the median models retained the principal monotonic, low-velocity-layer, and high-velocity-layer characteristics of Models A, B, and C, respectively. Because the best-fitting, median, and true models were visually indistinguishable at the scale of Figure 3, their differences are reported quantitatively in Table 3 rather than represented by additional overlapping curves. These results demonstrate that BHO provides stable recovery for the tested noise-free layered models, while the run-to-run variability increases with structural complexity.

3.2. Noisy synthetic inversions

Field surface-wave data are affected by environmental vibration, instrument response, random interference, near-surface heterogeneity, and frequency-dependent picking errors. Here, a controlled perturbation experiment was designed to evaluate the sensitivity of BHO to prescribed random data errors. Independent uniformly distributed perturbations with an amplitude based on 10% of the mean phase velocity were added to the theoretical dispersion curves of Models A–C. This simplified perturbation

Table 3. Best-fitting estimates and empirical distributions of the model parameters obtained from 20 independent noise-free inversions for Models A–C

Model	Parameter	True value	Best	Median	P5–P95
	V_{S1}	180.000	180.002	180.001	179.988–180.030
	V_{S2}	260.000	260.083	260.087	259.264–261.294
	V_{S3}	380.000	380.034	379.942	378.691–382.097
A	V_{S4}	560.000	559.999	559.993	559.889–560.069
	H_1	3.000	3.001	3.001	2.992–3.012
	H_2	4.000	4.003	4.002	3.970–4.065
	H_3	5.000	4.993	4.992	4.901–5.059
	V_{S1}	200.000	200.004	200.002	199.953–200.079
	V_{S2}	330.000	330.265	330.551	327.569–333.622
	V_{S3}	220.000	220.600	221.422	214.243–225.176
B	V_{S4}	560.000	560.028	560.029	559.753–560.336
	H_1	3.000	3.001	3.001	2.987–3.022
	H_2	5.000	4.973	4.927	4.735–5.225
	H_3	4.000	4.028	4.073	3.763–4.269
	V_{S1}	180.000	179.996	179.990	179.915–180.059
	V_{S2}	440.000	439.590	438.092	423.756–452.738
	V_{S3}	280.000	279.748	278.683	266.178–286.215
C	V_{S4}	600.000	599.990	599.956	599.650–600.298
	H_1	3.000	2.999	2.998	2.978–3.015
	H_2	4.000	4.011	4.056	3.708–4.544
	H_3	5.000	4.987	4.934	4.364–5.328

Note: V_S is expressed in m/s and H in m. Best denotes the solution with the lowest final objective-function value among the 20 independent runs. P5–P95 denotes the empirical 5th–95th percentile range and characterizes run-to-run variability rather than a formal Bayesian credible interval.

model is not intended to reproduce the full statistical characteristics of uncertainty in picked-field multichannel analysis of surface-wave dispersion curves. The resulting data were inverted with BHO, and the curve fits, recovered V_S structures, and parameter errors were evaluated (Figure 4 and Table 4). The perturbed data are defined as in **Equation 19**:

$$v_{i,0}^{\text{noisy}} = v_{i,0}^{\text{true}} + \frac{10\% \times \sum_{i=1}^{N_0} v_{i,0}^{\text{true}} \times \varepsilon_i}{N_0} \tag{19}$$

where $v_{i,0}^{\text{noisy}}$ is the perturbed phase velocity at frequency index i; $v_{i,0}^{\text{true}}$ is the corresponding noise-free value; N_0 is the number of valid fundamental-mode data points; and ε_i is an independent random variable uniformly distributed on [−1, 1].

After the 10% random perturbations were introduced, BHO still reproduced the overall dispersion trends for all three models (Figure 4). The 20 calculated curves remained relatively compact. The best-fitting solutions for Models A, B, and C were obtained in runs 13, 5, and 20, with final objective-function values of 7.05724, 8.5112, and 6.4985, respectively. For Model A, the median H and V_S values remained close to the true parameters. For Model B, the median estimates of V_{S2} and V_{S3} were 329.744 and 219.826 m/s, respectively, preserving the low-velocity third layer. For Model C, the corresponding median estimates were 439.256 and 279.633 m/s, preserving the high-velocity second layer and the subsequent velocity decrease.

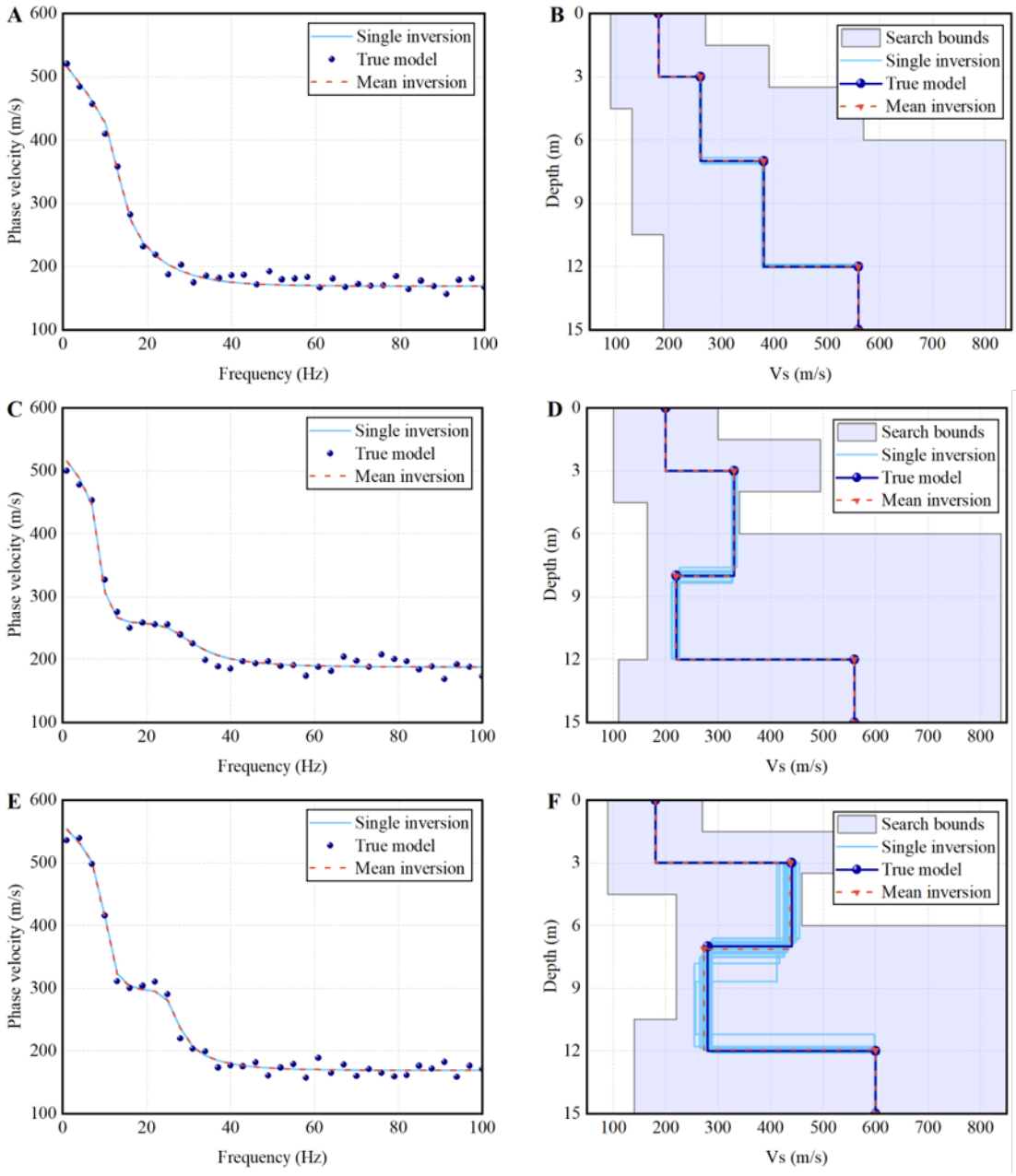

Figure 4. Inversion results for Models A–C under the prescribed 10% uniform-random perturbation model. (A, C, E) Dispersion curves; (B, D, F) Shear-wave velocity profiles.

The empirical parameter ranges show that the effects of random perturbations are parameter-dependent rather than uniform. Model A retained narrow parameter distributions, whereas Models B and C exhibited broader ranges for several intermediate-layer velocities and thicknesses. The largest spread occurred in Model C, particularly for V_{S2}, V_{S3}, H_2, and H_3, reflecting the greater variability associated with recovering its strong velocity reversal. Nevertheless, the true parameter values remained within the empirical 5th–95th percentile ranges for all three models, and the median models preserved their principal structural characteristics.

3.3. Joint multimode inversion

Measured dispersion images commonly contained energy ridges from the fundamental and one or more higher

Table 4. Best-fitting estimates and empirical distributions of the model parameters obtained from 20 independent noisy inversions for Models A–C

Model	Parameter	True value	Best	Median	P5–P95
A	V_{S1}	180.000	180.000	180.000	179.962–180.030
	V_{S2}	260.000	259.977	260.029	259.339–262.118
	V_{S3}	380.000	380.012	380.013	379.147–381.994
	V_{S4}	560.000	560.002	560.001	559.932–560.138
	H_1	3.000	3.000	3.000	2.991–3.022
	H_2	4.000	4.000	4.001	3.979–4.083
	H_3	5.000	5.002	4.997	4.813–5.055
B	V_{S1}	200.000	200.004	199.985	199.952–200.043
	V_{S2}	330.000	330.155	329.744	326.688–332.345
	V_{S3}	220.000	220.316	219.826	211.487–225.348
	V_{S4}	560.000	560.022	560.021	559.657–560.292
	H_1	3.000	3.001	2.998	2.983–3.012
	H_2	5.000	4.986	5.025	4.765–5.362
	H_3	4.000	4.015	3.982	3.612–4.257
C	V_{S1}	180.000	180.002	179.997	179.895–180.069
	V_{S2}	440.000	440.454	439.256	417.455–455.437
	V_{S3}	280.000	280.263	279.633	251.137–288.890
	V_{S4}	600.000	600.005	599.989	599.142–600.265
	H_1	3.000	3.001	2.999	2.968–3.017
	H_2	4.000	3.988	4.019	3.604–4.909
	H_3	5.000	5.014	4.980	3.879–5.473

modes. Higher-mode data provided complementary sensitivity to deeper structure and complex velocity variations. To test BHO under multimode constraints, fundamental-, first-higher-, and second-higher-mode data were generated for Model A. Two inversions were performed: the fundamental plus first higher mode, and the fundamental plus first and second higher modes. The synthetic dispersion curves were generated from the known Model A, and the modal branches were assumed to be correctly identified. Accordingly, this experiment evaluates BHO under ideal modal-assignment conditions and does not test its sensitivity to mode-picking or mode-identification errors. Figure 5 shows the dispersion fits and recovered V_S models, whereas Table 5 reports the true values, best-fitting estimates, component-wise medians, and empirical 5th–95th percentile ranges of the recovered parameters.

The BHO jointly fits the selected modes and recovers the reference V_S structure in both cases (Figure 5). For the fundamental and first-higher-mode inversion, the best-fitting solution was obtained in run 17, with a final objective-function value of 2.97×10^{-4}. For the fundamental, first, and second higher-mode inversions, run 2 produced the lowest final objective-function value of 1.98×10^{-4}. Under both configurations, the best-fitting and median parameter estimates were close to the true Model A values, and the principal interfaces and layer velocities were consistently recovered. Adding the second higher mode narrows the empirical 5th–95th percentile ranges of all seven inverted parameters (Table 5). Compared with the fundamental- and first-higher-mode inversions, these ranges decrease by approximately 45.5%–80.9%, with the largest reductions

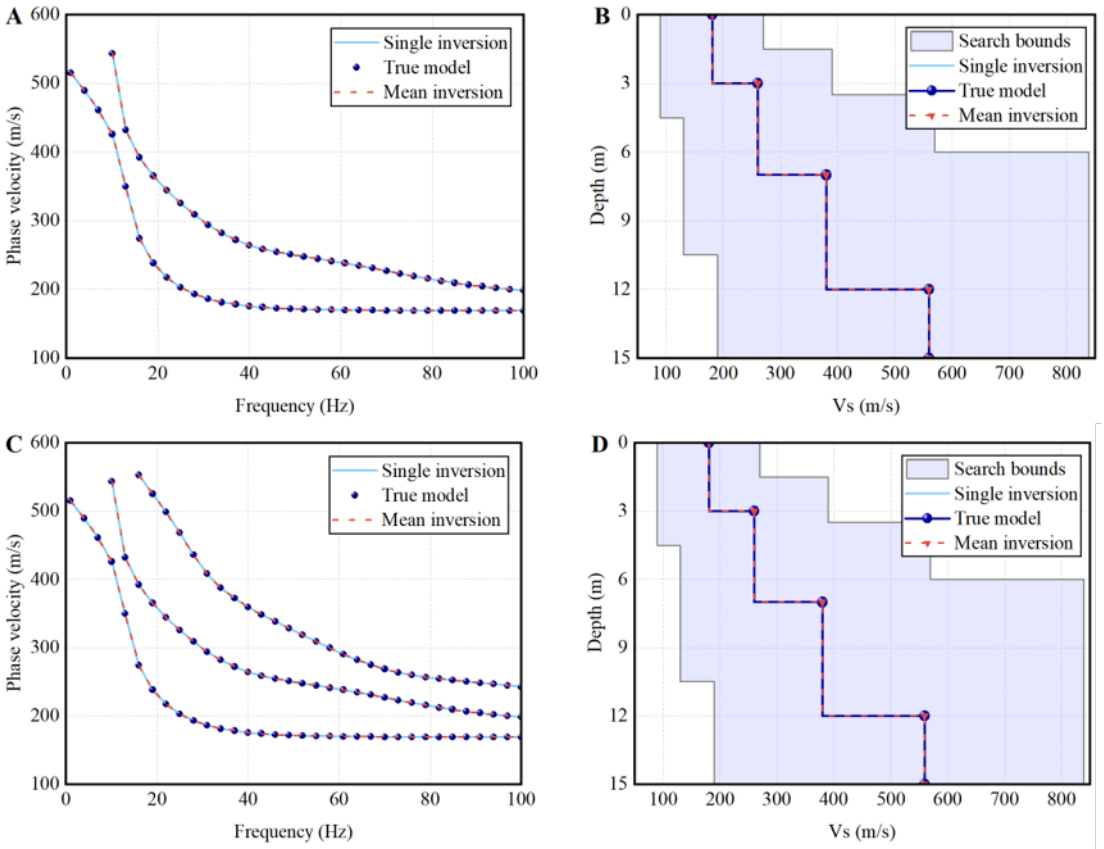

Figure 5. Multimode inversion of Model A. (A, C) Dispersion curves. (B, D) Shear-wave velocity profiles.

for V_{S3} and H_3. This systematic narrowing indicates that the additional modal information reduces run-to-run variability and provides stronger constraints on the Model A parameters under the tested noise-free conditions.

3.4. Comparison with other optimization algorithms

The BHO was compared with WOA, PSO, and APO using both noise-free and perturbed fundamental-mode data for Model A. Each algorithm used a population size of 30, a maximum of 200 iterations, and was run independently 20 times. The comparison considered recovery errors of V_S and layer thickness, the distributions of the final objective-function values, and computational cost. In Figure 6A and 6B, the blue line with circles is the true model, and the green-triangle, cyan-square, purple-triangle, and red-star curves show the PSO, APO, WOA, and BHO results, respectively. Figure 6C–F shows the distributions of the final objective-function values from the 20 noise-free runs of PSO, APO, WOA, and BHO, respectively, whereas Figure 6G–J shows the corresponding distributions for the perturbed data. Table 6 reports the model-recovery errors. Table 7 reports the best values, means, standard deviations, and medians of the final objective-function values from the 20 independent runs, together with the number of forward-model evaluations and the single-run wall-clock time of each algorithm. All timing tests were performed independently on the same computer equipped with an Intel Core Ultra 9 275HX processor and 32 GB DDR5 RAM.

The BHO produced the lowest and most concentrated final objective-function values in both tests (Figure 6C–J and Table 7). For the noise-free data, its best value, mean ± standard deviation, and median were 0.00250, 0.02184 ± 0.02010, and 0.00977, respectively. The corresponding mean values for PSO, APO, and WOA were 0.41661, 0.37985, and 1.26211, respectively. For the perturbed data, BHO yielded a best value of 7.05724, a mean ± standard deviation of $7.05725 \pm 1.79\times10^{-5}$, and a median of 7.05725. These values were lower and substantially less dispersed than those obtained using the other algorithms. The repeated-run results therefore show that the favorable BHO result was not produced by only an occasional exceptionally good run. However, BHO required 7,560 forward-model evaluations and 78.37 s for the representative run,

Table 5. Best-fitting estimates and empirical distributions of the model parameters obtained from 20 independent joint multimode inversions of Model A

Model	Parameter	True value	Best	Median	P5–P95
Fundamental + first higher mode	V_{S1}	180.0000	180.0003	179.9999	179.9968–180.0026
	V_{S2}	260.0000	260.0004	260.0005	259.9920–260.0108
	V_{S3}	380.0000	379.9928	380.0060	379.9637–380.0903
	V_{S4}	560.0000	559.9994	559.9997	559.9909–560.0138
	H_1	3.0000	3.0000	3.0000	2.9998–3.0003
	H_2	4.0000	3.9999	4.0001	3.9996–4.0012
	H_3	5.0000	4.9998	5.0004	4.9987–5.0022
Fundamental + first + second higher modes	V_{S1}	180.0000	179.9999	179.9996	179.9986–180.0018
	V_{S2}	260.0000	260.0001	259.9992	259.9956–260.0019
	V_{S3}	380.0000	380.0000	380.0002	379.9874–380.0156
	V_{S4}	560.0000	560.0003	560.0001	559.9969–560.0024
	H_1	3.0000	3.0000	3.0000	2.9999–3.0001
	H_2	4.0000	4.0000	4.0000	3.9997–4.0003
	H_3	5.0000	5.0001	5.0000	4.9997–5.0003

Note: Four decimal places are retained because the recovered parameter distributions are exceptionally narrow.

compared with 6,001–6,031 evaluations and 23.89–26.65 s for the other algorithms (Table 7). Thus, the improved accuracy and repeatability of BHO were accompanied by a higher computational cost under the tested settings.

Table 6. Model-recovery errors of the tested optimization algorithms for Model A

Algorithm	Noise–free velocity RE	Noise–free thickness RE	Perturbed velocity RE	Perturbed thickness RE
PSO	1.459E–2	6.360E–2	2.571E–2	6.955E–2
APO	1.885E–2	1.008E–1	1.561E–2	3.842E–2
WOA	9.550E–2	5.312E–2	1.047E–2	2.018E–2
BHO	4.433E–4	3.779E–3	2.168E–4	1.475E–3

Abbreviations: APO: Artificial protozoa optimizer; BHO: Bounty hunter optimizer; PSO: Particle swarm optimization; RE: Recovery error; WOA: Whale optimization algorithm.

3.5. Sensitivity to an overparameterized layer model

To examine the effect of an overparameterized layer model, we inverted the noise-free fundamental-mode dispersion data of Model A, generated from three finite-thickness layers over a half-space, using five finite-thickness layers over a half-space. The P-wave velocities and densities were kept fixed. Their values in the second finite layer of the generating model were repeated across three inversion sublayers, so that the enlarged parameterization could represent an equivalent generating model. The five thicknesses were bounded between 0.2 and 15 m, and the six shear-wave velocities between 50 and min (1,000, 0.99 $V_{P,i}$) m/s. Unlike the baseline synthetic tests, these broad search bounds were not defined as ±50% of each true parameter. This experiment therefore evaluates the specified overparameterized search setting rather than isolating layer number as the only changed factor. Figure 7 and Table 8 summarize the dispersion fits, recovered models, and parameter distributions across repeated runs for this experiment.

Twenty BHO runs were performed with a population of 30 and a maximum of 200 iterations. In Figure 7 and Table 8, all runs achieved a final fundamental-mode dispersion-

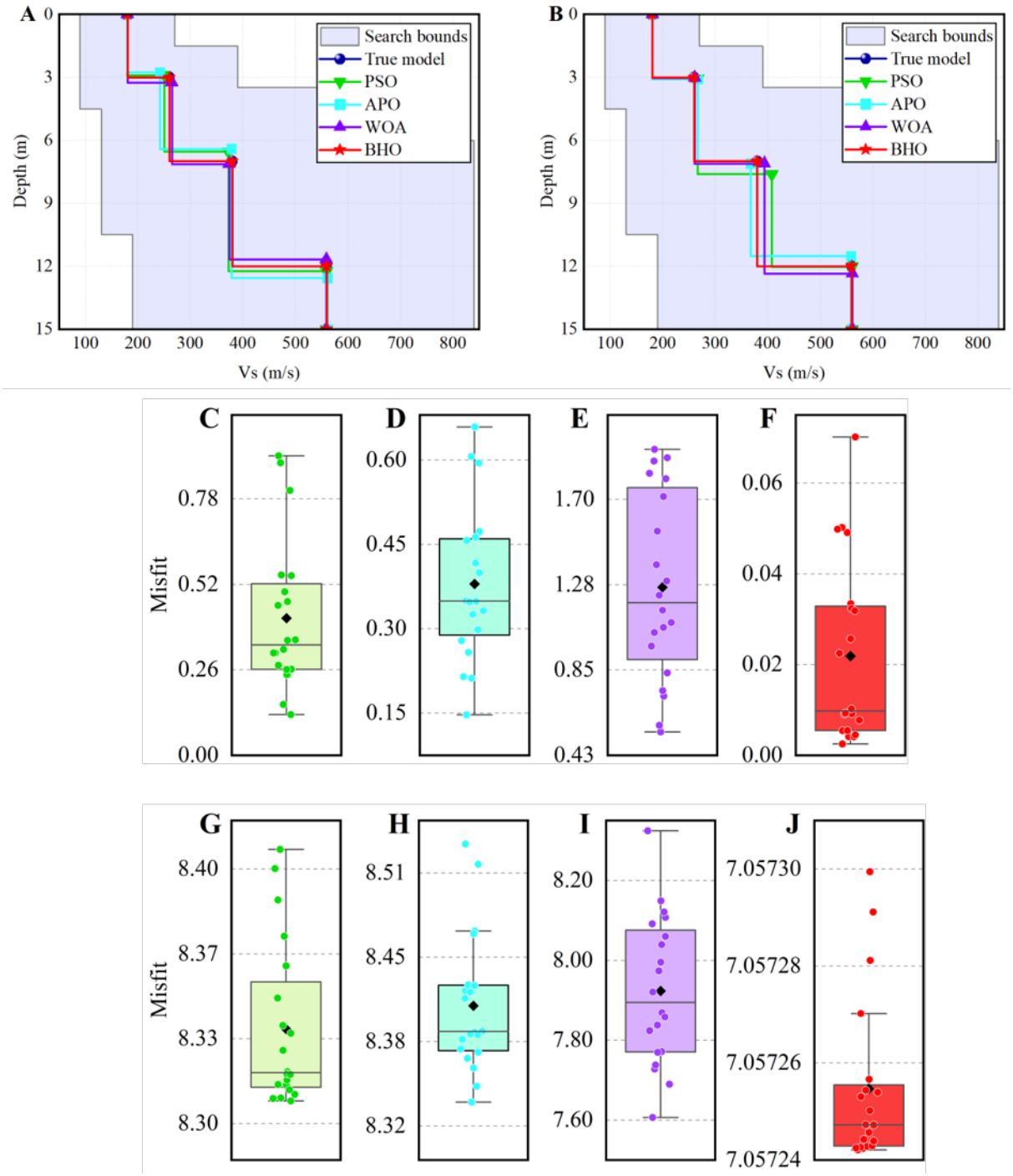

Figure 6. Comparison of the optimization algorithms for Model A. (A, B) recovered models for the noise-free and perturbed data, respectively. (C–F) Distributions of the final objective-function values obtained from 20 independent noise-free inversions using (C) PSO, (D) APO, (E) WOA, and (F) BHO. (G–J) Corresponding distributions obtained from 20 independent inversions of the perturbed data.

Abbreviations: APO: Artificial protozoa optimizer; ARO: Artificial rabbits optimization; BHO: Bounty hunter optimizer; FTO: Fourier transform optimization; NGO: Northern goshawk optimization; PSO: Particle swarm optimization; WOA: Whale optimization algorithm.

Table 7. Final objective statistics and computational costs of the tested optimization algorithms for Model A

Algorithm	Noise-free best	Noise-free mean ± SD	Noise-free median	Perturbed best	Perturbed mean ± SD	Perturbed median	NFE	Time (s)
PSO	0.12396	0.41661 ± 0.22781	0.33581	8.30433	8.33405 ± 0.03361	8.31596	6,030	26.65
APO	0.14707	0.37985 ± 0.13557	0.34929	8.33472	8.41026 ± 0.05351	8.38988	6,001	25.06
WOA	0.54112	1.26211 ± 0.46733	1.18519	7.60644	7.92363 ± 0.18527	7.89486	6,031	23.89
BHO	0.00250	0.02184 ± 0.0201	0.00977	7.05724	7.05725 ± 1.79E−5	7.05725	7,560	78.37

Note: Best, mean±standard deviation, and median were calculated from the final objective-function values of 20 independent runs. NFE and time denote the number of forward-model evaluations and the wall-clock time, respectively, for one representative run with a population size of 30 and 200 iterations. All timing tests were performed independently on the same computer. The reported times represent single-run measurements rather than runtime distributions.

Abbreviations: APO: Artificial protozoa optimizer; BHO: Bounty hunter optimizer; PSO: Particle swarm optimization; RE: Recovery error; SD: Standard deviation; WOA: Whale optimization algorithm.

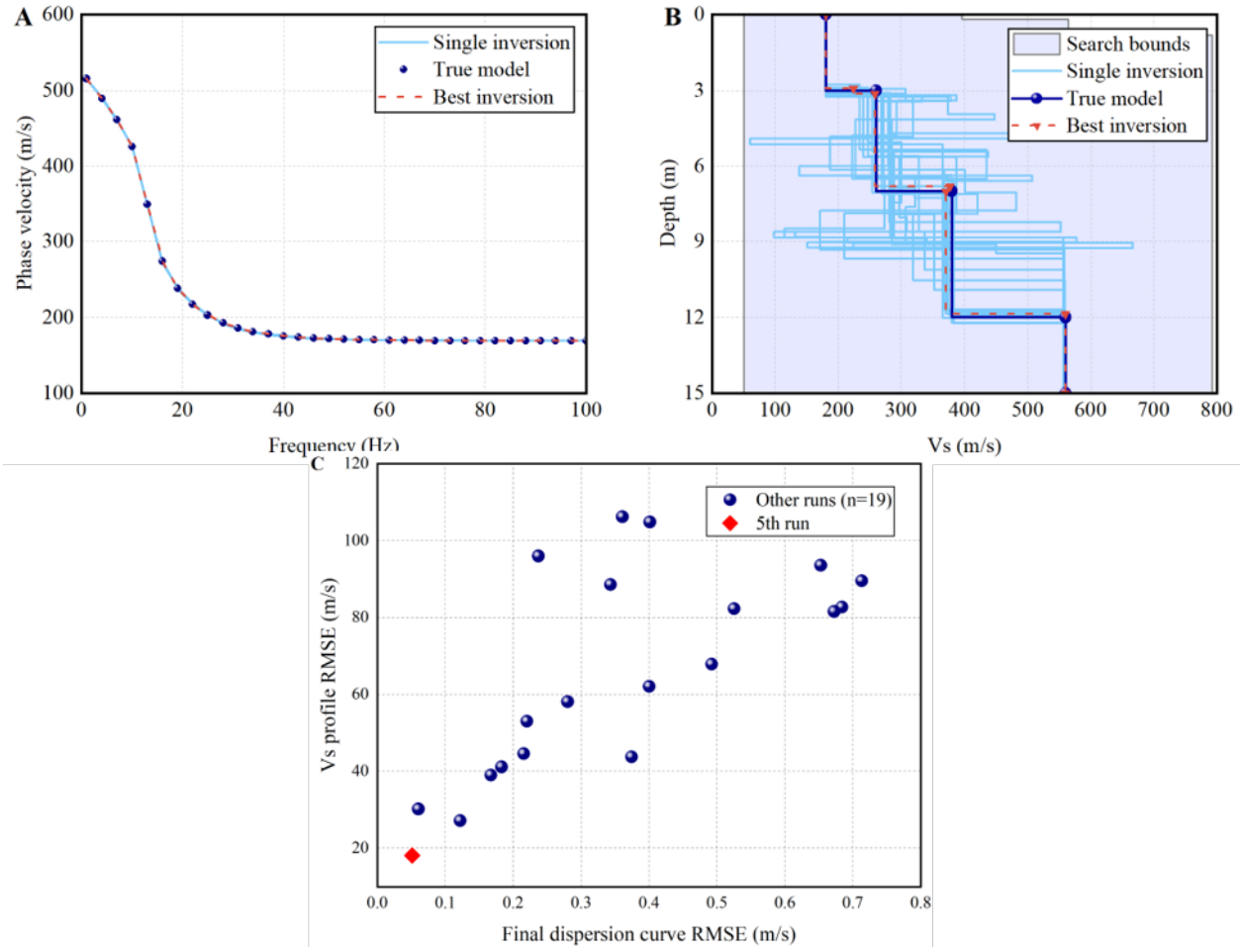

Figure 7. Overparameterized inversion of Model A: (A) Dispersion curves. (B) Shear-wave velocity profiles. (C) Final dispersion curve root mean square error (RMSE) and V_S profile RMSE for each run.

Table 8. Best-fitting run and empirical distributions for the overparameterized inversion of Model A

Quantity	Lowest-misfit run	Median	P5–P95
Dispersion curve root mean square error	0.0513	0.352	0.0559–0.6985
V_S profile root mean square error	18.16	64.99	22.66–105.55
H_1	2.925	3.134	2.836–3.252
H_2	0.2	2.195	0.200–4.248
H_3	3.683	1.243	0.200–4.552
H_4	0.22	0.523	0.200–3.612
H_5	4.831	2.225	0.200–6.358
V_{S1}	179.97	180.18	179.83–180.42
V_{S2}	224.18	280.02	229.07–383.26
V_{S3}	257.89	294.97	162.47–558.41
V_{S4}	377.69	297.9	74.28–494.75
V_{S5}	370.75	367.17	133.18–622.69
V_{S6}	560.01	559.04	557.32–560.03

curve RMSE below 1 m/s, with a median of 0.352 m/s. The best-fitting run, selected by the smallest dispersion-curve RMSE, yielded a dispersion RMSE of 0.0513 m/s and a V_S-profile RMSE of 18.16 m/s. Across all runs, however, the median profile RMSE was 64.99 m/s. Moreover, 18 of the 20 runs assigned at least one finite layer a thickness below 0.5 m, and several intermediate-layer parameters showed wide empirical ranges.

The close dispersion fits therefore did not imply stable recovery of the generating layer structure under this five-finite-layer parameterization. The model formed by averaging the 20 recovered parameter vectors had a dispersion-curve RMSE of approximately 6.92 m/s; consequently, we showed the lowest-misfit run together with the repeated-run distributions rather than treating the parameter-mean model as a representative solution. These empirical distributions describe sensitivity to stochastic optimization under the stated noise-free, fundamental-mode and fixed-property conditions. They are not posterior uncertainty intervals, and the experiment does not establish a layer-number-independent recovery capability.

4. Field-data application

Field data from Wyoming, United States, were used to evaluate practical applicability.[34] The survey employed 48 vertical-component geophones with an 8-Hz natural frequency and a 6.3-kg sledgehammer source. Receiver spacing and minimum offset were both 0.9 m. Figure 8A shows the shot gather, and Figure 8B shows the calculated dispersion image. Strong fundamental- and first-higher-mode ridges were visible. Inversions were therefore performed using the fundamental mode alone and using the fundamental plus first higher mode. A borehole V_S profile from the site provides an independent reference. On the basis of the available lithologic and velocity information, a five-layer parameterization was adopted. The fixed Poisson's ratios and densities and the search bounds for V_S and thickness are listed in Table 9.[34]

Table 9. Prior parameters and inversion bounds for the Wyoming field data

Layer	Prior information		Search bound	
	Poisson's ratio	ρ (g/cm^3)	V_S (m/s)	H (m)
1	0.38	2	100–300	1–5
2	0.38	2	100–400	1–5
3	0.35	2	100–600	1–5
4	0.35	2	200–600	1–5
5	0.30	2	200–800	∞

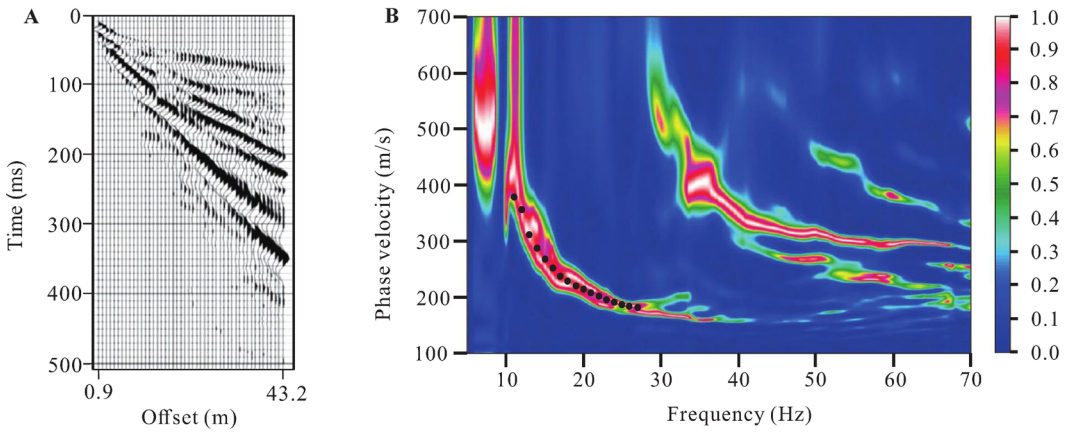

Figure 8. Wyoming field data. (A) Measured seismic record. (B) Dispersion-energy image.

Figure 9A shows the field dispersion fits. The purple curve shows the response from fundamental-mode inversion, the red curve shows the response from joint fundamental- and first-higher-mode inversion, and the black circles are the picked field data. Both strategies reproduce the observations, while the multimode response provides a closer overall match. Figure 9B shows the mean objective-function histories obtained from 20 independent BHO runs. The mean fundamental-mode history decreased rapidly and stabilized after approximately 50 iterations, whereas the mean multimode history stabilized after approximately 97 iterations. Neither mean history exhibited persistent oscillation or stagnation. Figure 9C compares the mean V_S profiles obtained from the 20 runs with the borehole model and the locally optimized result of Xia *et al.*[34] The mean fundamental-mode model reproduces the shallow (0–5 m) and deeper (11–14 m) trends but differs at some intermediate depths. The mean multimode model agrees more closely with the borehole profile between 0 and 13 m, particularly across the intermediate velocity changes, and is generally closer to the borehole information than the earlier local inversion. Figure 9D presents the borehole velocity interpretation. Table 10 further reports best-fitting estimate, component-wise median, and empirical 5th–95th percentile range for each inverted parameter. The best-fitting fundamental-mode and multimode models correspond to runs 8 and 17, respectively. The close agreement between the means and medians, together with the relatively compact empirical ranges, indicates consistent repeated-run convergence within the adopted five-layer model space. These results indicate that higher-mode constraints improve the recovery of the field V_S structure when the modal ridges can be identified reliably. Using higher-mode information to improve depth sensitivity and model resolution is consistent with established multichannel surface-wave inversion practice.[35]

5. Discussion

5.1. Inversion performance and bounty hunter optimizer search mechanisms

The tests show that BHO can navigate the nonlinear, multimodal objective functions encountered in Rayleigh-wave dispersion inversion. It produces low best values, means, and standard deviations for F_{12} and F_{13} and, for Model A, yields smaller velocity and thickness errors and lower objective values than PSO, APO, and WOA. These results are consistent with its search design. Oversampling and *K*-means clustering disperse the initial population; dynamic within-group roles coordinate broad exploration with local refinement; and Explorpolis filtering retains spatially complementary candidates. Together, these mechanisms improve exploration in a complex model space. A formal ablation study is still needed to quantify the contribution of each mechanism.

5.2. Effects of structural complexity and noise

The three synthetic models show that the run-to-run parameter distributions broaden as structural complexity increases. Under both noise-free and randomly perturbed conditions, the best-fitting and median models recover the principal characteristics of the monotonic, low-velocity-layer, and high-velocity-layer structures. The true parameter values remain within the empirical 5th–95th percentile ranges for all three models. The broadest ranges occur for the intermediate-layer velocities and thicknesses of Model C, indicating that strong velocity reversals and parameter coupling make these parameters less consistently resolved.

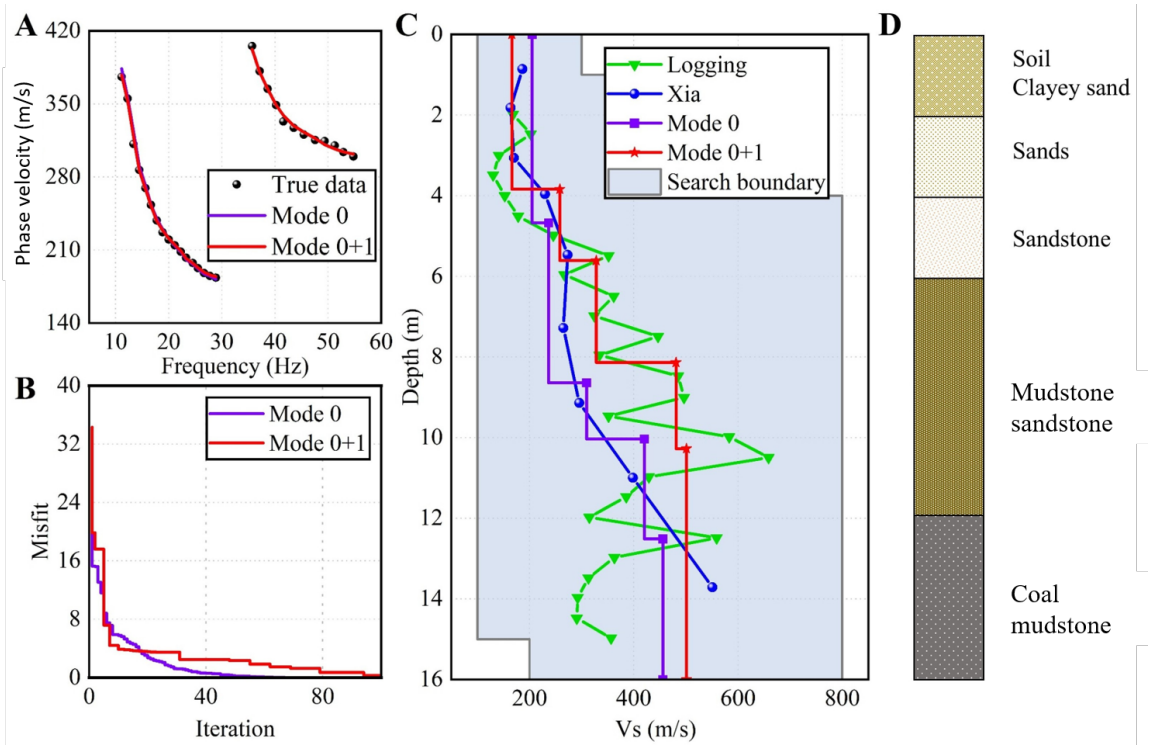

Figure 9. Field-data results. (A) dispersion-curve fits. (B) mean convergence histories calculated from 20 independent inversions. (C) mean V_S profiles calculated from 20 independent inversions. (D) Borehole information.

Table 10. Summary statistics of the field-data inversion parameters obtained from 20 independent bounty hunter optimizer runs

Model	Parameter	Best	Median	P5–P95
Fundamental mode	V_{S1}	205.17021	204.82314	202.69666–207.26956
	V_{S2}	237.13921	236.35355	234.66557–238.81113
	V_{S3}	309.85542	309.11345	307.45688–311.63022
	V_{S4}	420.52988	420.22335	417.73087–422.80383
	V_{S5}	454.7232	456.08145	453.25557–458.48653
	H_1	4.73897	4.67406	4.60219–4.74593
	H_2	3.95474	3.96603	3.89416–4.03790
	H_3	1.41842	1.39118	1.30083–1.48175
	H_4	2.45658	2.46112	2.40683–2.55739
Fundamental + first higher mode	V_{S1}	163.43753	166.01856	163.45225–168.58487
	V_{S2}	259.40353	258.38922	255.62539–261.15305
	V_{S3}	326.45892	328.17489	325.39464–330.95514
	V_{S4}	479.69528	481.21435	478.60351–483.82519
	V_{S5}	498.63119	501.1008	498.47425–503.72735
	H_1	3.80474	3.83906	3.77562–3.90250
	H_2	1.70772	1.76959	1.69626–1.84292
	H_3	2.45937	2.52713	2.45902–2.59524
	H_4	2.10799	2.13667	2.06551–2.20783

Because the 20 inversions used the same data, layer parameterization, search bounds, and objective function, their spread primarily characterizes stochastic variability between independent BHO runs under the adopted inversion configuration. The compact ensembles indicate consistent convergence within this predefined model space. However, repeated optimization does not replace posterior sampling and cannot independently quantify the full non-uniqueness of the inverse problem. Distinct clusters of similarly well-fitting models would suggest convergence to different solution basins, but the absence of such clusters under the present parameterization does not establish that the inverse solution is unique.

5.3. Multimode constraints and field-data performance

The multimode tests show that higher modes provide complementary constraints on the velocity structure. Adding the second higher mode to the fundamental and first higher modes narrowed the empirical 5th–95th percentile ranges of all seven Model A parameters by approximately 45.5%–80.9%. This systematic reduction indicates lower run-to-run variability and stronger parameter constraints under the tested noise-free conditions with correctly identified modal branches. These results show that BHO can use complementary multimode information under ideal modal-assignment conditions, but they do not establish its robustness to mode-picking or mode-identification errors. Moreover, these empirical ranges summarize variability among independent optimization runs and should not be interpreted as Bayesian credible intervals or as a formal posterior quantification of model non-uniqueness.

For the Wyoming data, the mean fundamental-mode model obtained from 20 independent runs reconstructs the shallow and part of the deeper velocity variation, whereas the mean fundamental-plus-first-higher-mode model agrees more closely with the borehole profile over 0–13 m. Figure 9C and Table 10 show similar mean and median estimates and relatively compact empirical parameter ranges, indicating good run-to-run repeatability within the adopted five-layer parameterization. The mean multimode convergence history stabilizes after about 97 iterations, compared with about 50 iterations for the fundamental mode. However, the modal picks are treated as correctly identified, whereas picking errors, mode mixing, mode kissing, or incorrect modal assignments may bias the recovered model. Therefore, the empirical distributions characterize optimizer variability but do not establish solution uniqueness or robustness to mode-identification errors. The improved borehole agreement is encouraging for this data set, but the potential accuracy gains must be weighed against computational cost, model parameterization, and the reliability of modal identification.

5.4. Limitations and future work

Several limitations remain. First, all forward calculations and inversions in this study assume one-dimensional, horizontally layered, isotropic elastic media. This controlled configuration provides a baseline for isolating and evaluating the search performance of BHO, but it does not account for direction-dependent elastic properties. Elastic anisotropy can alter Rayleigh-wave dispersion and may bias the shear-wave velocity and layer-thickness estimates obtained using an isotropic model.[36] The present results should therefore not be generalized to strongly anisotropic formations. Future work should couple BHO with an anisotropic forward solver, such as a Cauchy-based formulation, and evaluate the recovery of direction-dependent elastic parameters. Two-dimensional or pseudo-two-dimensional models are also needed to assess structural resolution in the presence of lateral heterogeneity, velocity gradients, and irregular interfaces. Second, the present noise experiment uses independent, uniformly distributed perturbations with amplitudes based on the mean phase velocity. This controlled design provides a test of algorithmic robustness but does not reproduce the full uncertainty structure of picked field dispersion curves. In field applications, picking errors are commonly frequency-dependent and may become more pronounced at low frequencies. Missing picks, outliers, mode mixing, mode kissing, and mode misidentification may further affect the inversion. Moreover, the present multimode objective assigns equal weight to each valid mode-frequency observation and does not explicitly account for differences in data uncertainty or picking reliability among frequencies and modes. Future work should therefore evaluate BHO using frequency-dependent uncertainty models, incomplete dispersion curves, outliers, and uncertain mode assignments, and investigate frequency- and mode-dependent weighting based on data quality and picking uncertainty.

The algorithm comparison used equal population sizes and iteration limits, but the resulting computational costs were not equal. BHO required 7,560 forward-model evaluations and 78.37 s in the representative run, whereas PSO, APO, and WOA required 6,001–6,031 evaluations and 23.89–26.65 s. The present results therefore demonstrate an accuracy–cost trade-off rather than superior efficiency under an equal computational budget. Moreover, the reported wall-clock times were obtained from single representative runs and may be affected by implementation and system conditions. Future comparisons should impose a common forward-evaluation budget and report runtime

distributions from repeated timing tests. The empirical repeated-run ranges reported here are not posterior uncertainty intervals. Formal posterior sampling or confidence-interval analyses are needed to quantify model uncertainty more rigorously, and ablation experiments are still warranted to isolate the contributions of individual BHO mechanisms. Applications to additional geological settings, and joint inversion with other geophysical observations or geological constraints, are also required before broad practical generalization.

6. Conclusion

Rayleigh-wave dispersion inversion is nonlinear, coupled, and non-unique, and population-based algorithms may struggle to balance exploration and local convergence in complex model spaces. This study introduces BHO for dispersion inversion and evaluates it with penalized benchmark functions, three synthetic structures, noisy and multimode data, algorithm comparisons, and a field example. The main findings are as follows.

(i) BHO combines oversampling and *K*-means initialization with cooperative group search, dynamic task allocation, Explorpolis filtering, and QPRS reassignment. It produces lower best values, means, and standard deviations than the compared algorithms for F_{12} and F_{13}, providing a numerical basis for its use in nonlinear dispersion inversion.

(ii) BHO recovers the principal interfaces and velocity variations of the monotonic, low-velocity-layer, and high-velocity-layer models under both noise-free and randomly perturbed conditions. The median models preserve the principal structural characteristics, and the true parameter values remain within the empirical 5th–95th percentile ranges of all three models. The broader ranges obtained for the more complex intermediate layers indicate increased run-to-run variability.

(iii) Higher-mode information strengthens the constraints on the model parameters. Adding the second higher mode narrows the empirical 5th–95th percentile ranges of all seven Model A parameters by approximately 45.5%–80.9%, demonstrating improved consistency among independent BHO runs under the tested multimode configuration. The results demonstrate that BHO can use complementary multimode information under ideal modal-assignment conditions, while its sensitivity to mode-picking and mode-identification errors remains to be evaluated.

(iv) For Model A, BHO yielded the lowest best, mean, and median final objective-function values and the smallest standard deviations across 20 independent runs under both noise-free and perturbed conditions. Its improved accuracy and repeatability were accompanied by a higher computational cost, requiring 7,560 forward-model evaluations and 78.37 s in the representative run, compared with 6,001–6,031 evaluations and 23.89–26.65 s for the other algorithms. For the Wyoming data, the fundamental-plus-first-higher-mode model agrees well with the borehole V_S structure between 0 and 13 m and improves the intermediate-depth recovery. The close agreement between the means and medians, together with the relatively compact empirical parameter ranges, indicates consistent repeated-run recovery within the adopted five-layer parameterization.

These conclusions apply only to the one-dimensional isotropic layered models and data examined here. The present study should therefore be regarded as a baseline for extending BHO-based dispersion inversion to more general anisotropic media. Future work should address lateral heterogeneity, frequency-dependent picking uncertainty, missing dispersion data, outliers, mode-identification errors, equal-budget algorithm comparisons, ablation studies, and quantitative uncertainty analysis.

Acknowledgments

None.

Funding

This work was supported by research funding from PowerChina Huadong Engineering Co., Ltd.

Conflict of interest

The authors declare no potential conflict of interest.

Author contributions

Conceptualization: Zhiying Liao, Miaojun Sun
Formal analysis: Ping Xu
Investigation: Ping Xu, Jian Xu
Methodology: Zhiying Liao, Miaojun Sun
Writing–original draft: Zhiying Liao
Writing–review & editing: Jian Xu, Miaojun Sun

Availability of data

Data are available from the corresponding author upon reasonable request.

AI tools statement

OpenAI Codex (GPT-6.1 Terra) was used to assist with language editing and formatting checks during revision. No new numerical results were generated using this tool. The authors remain responsible for the scientific content

and its final verification.

References

1. Rayleigh L. On waves propagated along the plane surface of an elastic solid. *Proc Lond Math Soc*. 1885;s1-17(1):4-11.

   doi: 10.1112/plms/s1-17.1.4

2. Thomson WT. Transmission of elastic waves through a stratified solid medium. *J Appl Phys*. 1950;21(2):89-93.

   doi: 10.1063/1.1699629

3. Haskell NA. The dispersion of surface waves on multilayered media. *Bull Seismol Soc Am*. 1953;43(1):17-34.

   doi: 10.1785/BSSA0430010017

4. Schmidt H, Tango G. Efficient global matrix approach to the computation of synthetic seismograms. *Geophys J R Astron Soc*. 1986;84(2):331-359.

   doi: 10.1111/j.1365-246X.1986.tb04359.x

5. Chen X. A systematic and efficient method of computing normal modes for multilayered half-space. *Geophys J Int*. 1993;115(2):391-409.

   doi: 10.1111/j.1365-246X.1993.tb01194.x

6. Kuznetsov SV. Cauchy six-dimensional formalism for Lamb waves in multilayered plates. *ISRN Mech Eng*. 2013;2013:1-11.

   doi: 10.1155/2013/698706

7. Aki K. Space and time spectra of stationary stochastic waves, with special reference to microtremors. *Bull Earthq Res Inst*. 1957;35(3):415-456.

8. Park CB, Miller RD, Xia J. Multichannel analysis of surface waves. *Geophysics*. 1999;64(3):800-808.

   doi: 10.1190/1.1444590

9. Xia J, Miller RD, Park CB. Estimation of near-surface shear-wave velocity by inversion of Rayleigh waves. *Geophysics*. 1999;64(3):691-700.

   doi: 10.1190/1.1444578

10. Foti S, Lai CG, Rix GJ, Strobbia C. *Surface Wave Methods for Near-Surface Site Characterization*. Boca Raton, FL: CRC Press; 2014.

    doi: 10.1201/b17268

11. Socco LV, Foti S, Boiero D. Surface-wave analysis for building near-surface velocity models—established approaches and new perspectives. *Geophysics*. 2010;75(5):75A83-75A102.

    doi: 10.1190/1.3479491

12. Foti S, Hollender F, Garofalo F, *et al*. Guidelines for the good practice of surface wave analysis: a product of the InterPACIFIC project. *Bull Earthq Eng*. 2018;16(6):2367-2420.

    doi: 10.1007/s10518-017-0206-7

13. Vantassel JP, Cox BR. SWinvert: a workflow for performing rigorous 1-D surface wave inversions. *Geophys J Int*. 2021;224(2):1141-1156.

    doi: 10.1093/gji/ggaa426

14. Li J, Feng Z, Schuster GT. Wave-equation dispersion inversion. *Geophys J Int*. 2017;208(3):1567-1578.

    doi: 10.1093/gji/ggw465

15. Kausel E, Roësset JM. Stiffness matrices for layered soils. *Bull Seismol Soc Am*. 1981;71(6):1743-1761.

    doi: 10.1785/BSSA0710061743

16. Dorman J, Ewing M. Numerical inversion of seismic surface wave dispersion data and crust-mantle structure in the New York-Pennsylvania area. *J Geophys Res*. 1962;67(13):5227-5241.

    doi: 10.1029/JZ067i013p05227

17. Constable SC, Parker RL, Constable CG. Occam's inversion: a practical algorithm for generating smooth models from electromagnetic sounding data. *Geophysics*. 1987;52(3):289-300.

    doi: 10.1190/1.1442303

18. Tarantola A. *Inverse Problem Theory and Methods for Model Parameter Estimation*. Philadelphia, PA: Society for Industrial and Applied Mathematics; 2005.

    doi: 10.1137/1.9780898717921

19. Wathelet M, Jongmans D, Ohrnberger M. Surface-wave inversion using a direct search algorithm and its application to ambient vibration measurements. *Near Surf Geophys*. 2004;2(4):211-221.

    doi: 10.3997/1873-0604.2004018

20. Wathelet M. An improved neighborhood algorithm: parameter conditions and dynamic scaling. *Geophys Res Lett*. 2008;35(9):L09301.

    doi: 10.1029/2008GL033256

21. Sambridge M. Geophysical inversion with a neighbourhood algorithm—I. Searching a parameter space. *Geophys J Int*. 1999;138(2):479-494.

    doi: 10.1046/j.1365-246x.1999.00876.x

22. Sen MK, Stoffa PL. Nonlinear one-dimensional seismic waveform inversion using simulated annealing. *Geophysics*. 1991;56(10):1624-1638.

    doi: 10.1190/1.1442973

23. Lomax A, Snieder R. Finding sets of acceptable solutions with a genetic algorithm with application to surface wave group dispersion in Europe. *Geophys Res Lett*. 1994;21(24):2617-2620.

    doi: 10.1029/94GL02635

24. Zarean A, Mirzaei N, Mirzaei M. Applying MPSO for

building shear wave velocity models from microtremor Rayleigh-wave dispersion curves. *J Seism Explor*. 2015;24(1):51-82.

doi: 10.36922/JSE281

25. Poormirzaei R, Hamidzadeh Moghadam R, Zarean A. The application of PSO to joint inversion of microtremor Rayleigh waves dispersion curves and refraction traveltimes. *J Seism Explor*. 2015;24(4):305-325.

doi: 10.36922/JSE263

26. Lei Y, Shen H, Xie S, Li Y. Rayleigh wave dispersion curve inversion combining with GA and DSL. *J Seism Explor*. 2018;27(2):151-165.

doi: 10.36922/JSE187

27. Duan Z, Yan J, Liu S, Zheng F. Rayleigh-wave dispersion curve inversion based on the mantis shrimp optimization algorithm. *J Seism Explor*. 2026;35(5):026170074.

doi: 10.36922/jse026170074

28. Yu M, Yang H, Zhang J, *et al*. Bounty hunter optimizer: a novel metaheuristic with an application to multi-UAV mobile edge computing and path planning. *Knowl Based Syst*. 2026;341:115836.

doi: 10.1016/j.knosys.2026.115836

29. Wang X, Snášel V, Mirjalili S, Pan JS, Kong L, Shehadeh HA. Artificial protozoa optimizer (APO): a novel bio-inspired metaheuristic algorithm for engineering optimization. *Knowl Based Syst*. 2024;295:111737.

doi: 10.1016/j.knosys.2024.111737

30. Mirjalili S, Lewis A. The whale optimization algorithm. *Adv Eng Softw*. 2016;95:51-67.

doi: 10.1016/j.advengsoft.2016.01.008

31. Dehghani M, Hubálovský Š, Trojovský P. Northern goshawk optimization: a new swarm-based algorithm for solving optimization problems. *IEEE Access*. 2021;9:162059-162080.

doi: 10.1109/ACCESS.2021.3133286

32. Saad MR, Emam MM, Hosney ME, Samee NA, Alkanhel RI, Houssein EH. Fourier transform optimizer: a novel physics-inspired metaheuristic algorithm for optimization problems. *Knowl Based Syst*. 2026;340:115651.

doi: 10.1016/j.knosys.2026.115651

33. Wang L, Cao Q, Zhang Z, Mirjalili S, Zhao W. Artificial rabbits optimization: a new bio-inspired meta-heuristic algorithm for solving engineering optimization problems. *Eng Appl Artif Intell*. 2022;114:105082.

doi: 10.1016/j.engappai.2022.105082

34. Xia J, Miller RD, Park CB, Wightman E, Nigbor R. A pitfall in shallow shear-wave refraction surveying. *J Appl Geophys*. 2002;51(1):1-9.

doi: 10.1016/S0926-9851(02)00197-0

35. Xia J. Estimation of near-surface shear-wave velocities and quality factors using multichannel analysis of surface-wave methods. *J Appl Geophys*. 2014;103:140-151.

doi: 10.1016/j.jappgeo.2014.01.016

36. Zhang SX, Wang Y, Zhou HW, Chan LS. Dispersion splitting of Rayleigh waves in layered azimuthally anisotropic media. *J Appl Geophys*. 2009;67(2):130-142.

doi: 10.1016/j.jappgeo.2008.10.008